Fabrication of flexible blade models from a silicone-based polymer to test the effect of surface corrugations on drag and blade motion

M. Fryer,* D. Terwagne, P. M. Reis, H. Nepf
Department of Civil and Environmental Engineering, Massachusetts Institute of Technology (MIT), Cambridge, Massachusetts

Abstract

Macrocystis blades develop longitudinal corrugations in regions with strong current and wave action. This study examined the effect of corrugations on blade motion and blade drag by constructing flexible blades with different corrugation amplitude and a control blade with no corrugation. The models were designed to be dynamically and geometrically similar to natural blades. Acrylic molds were etched using a laser cutter and filled with a silicone-based polymer to create flexible model blades with sinusoidal corrugations. The corrugated and flat model blades were tested in a water channel using drag force measurements and video analysis. The corrugated blades experienced a drag per surface area reduction of up to 60% compared to the flat blade. Additionally, the corrugated models exhibited smaller motion, as quantified by the maximum vertical displacement. The reduction in drag may explain why corrugations are observed in exposed regions of high current and wave action, where a reduction in drag provides important protection against breakage.

Through phenotype plasticity, the morphology of kelp blades changes in response to environmental stimuli, such as variations in nutrient availability and hydrodynamic conditions (Hurd 2000). By transplanting live plants to sites with different environmental conditions, studies have shown that the blade geometric parameters such as length, width, thickness, and overall shape can change within the timescale of the kelp life cycle (Norton 1969; Druehl and Kemp 1982). Since kelp and other macroalgae are frequently the dominant producers in coastal regions, providing shelter and nutrients to other organisms in their ecosystem (Hurd 2000), there is incentive to understand how specific morphologies enhance plant survival in various environmental conditions.

The environmental settings associated with morphological change are commonly divided into "sheltered" and "exposed" conditions, referring to relatively lower and higher current and wave exposure, respectively (e.g., Hurd et al. 1996). The morphological changes are hypothesized to either enhance nutrient flux to the kelp surface or reduce hydrodynamic drag (Koehl et al. 2008). For example, Koehl et al. (2008) observed that *Nereocystis* blades exhibit ruffles or undulations in sheltered regions, compared to exposed regions where blades are flat. The ruffles increase blade movement, which can renew the water near the blade surface, which in turn can enhance nutrient flux (Koehl and

Alberte 1988; Huang et al. 2011). However, the ruffles also increase drag force, which can put the blade at risk of breaking in exposed regions (Koehl and Alberte 1988).

Although differences between sheltered and exposed blade morphology are not always observed in *Macrocystis* (Hepburn et al. 2007), generally the blades are thicker and have longitudinal corrugations in exposed regions (Fig. 1), and are thinner and exhibit little or no corrugations in sheltered regions (Hurd and Pilditch 2011, summarized here in Table 1). Hurd et al. (1997) suggested that the corrugations reduce skin friction, because similar longitudinal grooves (called riblets) have been observed to reduce skin friction by 7–8% on rigid surfaces by reducing the impact of span-wise boundary-layer vortices for a particular range of riblet spacing (Djenidi et al. 1994). Previous studies of corrugation in metal sheets have also shown that corrugation can enhance rigidity (Briassoulis 1986). Based on this, Rominger and Nepf (2014) hypothesized that the kelp corrugations enhance blade rigidity, which in turn reduces peak forces. Specifically, Rominger and Nepf (2014) showed that in some flow conditions, increasing blade rigidity significantly reduced drag by limiting the blade motion that occurs in response to flow oscillation (e.g., turbulence or waves). The degree of blade motion in response to flow can be characterized by the following non-dimensional force ratio of blade rigidity (resistance to bending) to fluid forcing (Michelin et al. 2008):
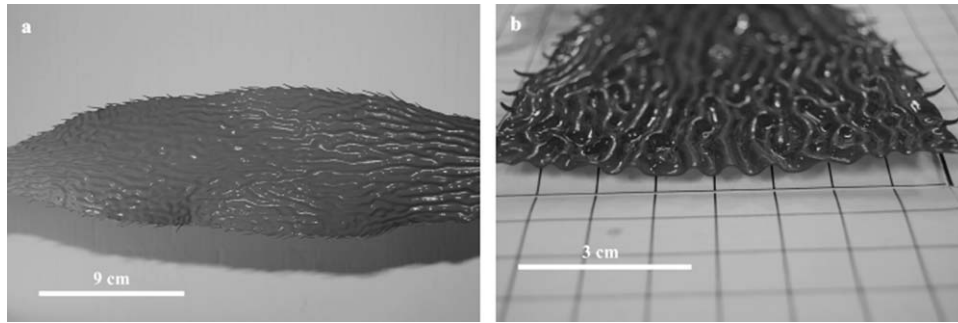
*Correspondence: mfryer@mit.edu

Fig. 1. (a) A photo of a *Macrocystis* blade, showing the longitudinal corrugations running along the length of the blade. (b) A cut section of a *Macrocystis* blade, showing the regularity of the corrugation wavelength and amplitude. (Photo credit: Rominger and Nepf 2014).

Table 1. Measurements of *Macrocystis* blade morphology from exposed and sheltered sites from Hurd and Pilditch (2011). The standard deviation of each measurement is given in parentheses. The elastic modulus of algal material was reported by Hale (2001).

	Exposed morphology	Sheltered morphology
Blade thickness, h (mm)	0.46 (0.07)	0.42 (0.13)
Elastic modulus, E (Pa)	5×10^6	5×10^6
Blade length, l (m)	0.62 (0.05)	0.52 (0.03)
Corrugation amplitude, a (mm)	1.4 (0.2)	—
Corrugation wavelength, λ (mm)	3.07 (0.15)	—

$$\eta = \frac{EI}{\rho_f b U^2 l^3}, \tag{1}$$

where E is the Young's modulus, I is the area moment of inertia, ρ_f is the density of the fluid, U is the streamwise velocity, and b, h and l are the width, thickness and length of the blade, respectively.

Rominger and Nepf (2014) created six flat blade models with a range of η between 10^{-6} and 10 by varying the material (high and low density polyethylene, and aluminium) and the model blade thickness (h). They found that below $\eta = 10^{-4}$, both the mean and instantaneous drag forces on the model blade increased rapidly with decreasing non-dimensional rigidity (η). The instantaneous peaks in drag, which can tear blades, were associated with inertial forces created by the large-amplitude flapping motions of the blade. Rominger and Nepf (2014) also showed that the range of η values over which blade drag is most sensitive to blade rigidity ($\eta < 10^{-4}$) corresponds to the range of η values exhibited in real kelp blades in coastal environments. Therefore, for real blades in the field, changes in morphology that increase blade rigidity are expected to reduce drag.

In this study, we test the hypothesis of Rominger and Nepf (2014) that corrugations reduce drag by increasing rigidity, which in turn decreases blade motion. We have developed a method to fabricate dynamically and geometrically scaled model blades with different degrees of realistic corrugation using etched acrylic molds. Synthetic models are useful for studying kelp because they are easier to maintain, allow for more control over parameters, and are not geographically limited to the regions where kelp grows. Several previous studies have also used scaled, laboratory models to develop a better understanding of blade-flow interaction. For example, Denny and Roberson (2002) used rigid copper models molded using plaster casts of real kelp blades to study the impact of blade motion on flux, using heat as a surrogate for nutrients. Denny et al. (1998) used a spring-mass system to study inertial forces on flexible plants such as kelp. Rosman et al. (2013) created a scaled model of an entire kelp forest in a laboratory flume using plastic sheets with a similar density to kelp. The models fabricated in this study reproduce both the flexibility and buoyancy of real kelp blades and can be designed to match any surface morphology. Our method is useful because the models more accurately represent real kelp blades and can be used to test a wider range of blade parameters. To assess both our fabrication method and the drag-reducing effects of corrugations, we measured the drag on each model blade when exposed to the same flow conditions in a water channel and used video analysis to observe the effects of corrugation on the motion of the blade.

Materials and procedures

We designed and fabricated three model kelp blades: one flat blade and two blades with sinusoidal corrugations running parallel to the streamwise length of the blade, with different amplitudes. The model blades were made from a silicone-based polymer and cast using laser-cut acrylic molds (more details provided below). The three models had the same length l, width b, and sheet thickness h, and were fabricated from the same material, so that they had the same

a) Side view of blade in channel

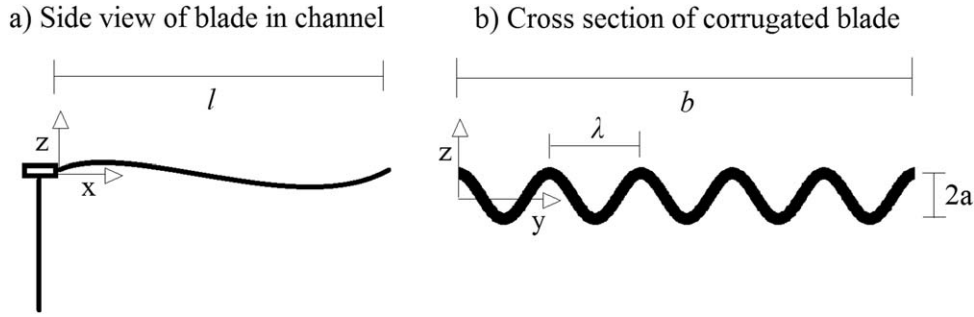## b) Cross section of corrugated blade

Fig. 2. (a) Sketch of blade attached to clamp from the side view. Flow in the channel moves in the *x*-direction. (b) Cross section of a corrugated model blade perpendicular to flow. The area moment of inertia *I* is defined about the *y*-axis.

elastic modulus, *E*. The design parameters were chosen using three constructs: First, working under the hypothesis that kelp blades develop corrugated morphologies in regions where changes in blade rigidity have the greatest effect on drag force, each blade was designed to be within the critical range $\eta < 10^{-4}$. According to Rominger and Nepf (2014), this is the range over which variation in rigidity has the most significant effect on drag. Second, the ratio of blade thickness to corrugation wavelength and amplitude should mimic what has been observed in actual kelp blades (Fig. 1; Table 1). Third, the model parameters were limited by the resolution and total size of the fabrication tools. Specifically, the molds were fabricated using a LaserPro Spirit GX laser cutter with a bed size of 46 cm × 81 cm and an *x-y* resolution of 0.1 mm.

The flat blade can be approximated as a rectangular beam, for which the area moment of inertia about the horizontal axis perpendicular to blade length (*y*-axis in Fig. 2) is

$$I = \frac{bh^3}{12} \tag{2}$$

For the corrugated models, the area moment of inertia can be approximated as

$$I = \frac{ba^2h}{2}\left(1 + \frac{\pi^2 a^2}{2\lambda^2}\right) \tag{3}$$

where *a* is the amplitude of the corrugation, and λ is the wavelength of corrugation, as shown in Fig. 2b (Lau 1981). The blades were made from a silicone-based elastomer, vinyl-polysiloxane (VPS), which is available in a range of elastic moduli. Specifically, we used a VPS (Zhermack Elite Double 8) with a Young's modulus of $E = 0.23 \pm 0.01$ MPa. This material is prepared by mixing equal parts base and catalyst in liquid form, after which polymerization occurs in approximately 20 min. To reach a non-dimensional force ratio (η) in the scaled-down model blade that was comparable to real kelp blades, the elastic modulus (*E*) was intentionally chosen to be less than that of real blades ($E = 5$ MPA, Table 1). The VPS has a density of 1024 ± 20 kg/m^3, so that the models were somewhat buoyant, which is consistent with real blades ($\rho = 1040$ kg/m^3, Hale 2001).

The flat model was designed to have a value of $\eta \approx 10^{-5}$ in a current of $U_\infty = 20$ cm/s (*see* Eq. 1). To meet that target, we set length $l = 30.0 \pm 0.1$ cm, width $b = 3.0 \pm 0.1$ cm, and thickness $h = 0.75 \pm 0.01$ mm, with the uncertainty representing the measurement uncertainty of the completed blade. These dimensions were held constant for all three blades. For geometric similarity, the corrugated model blades were constructed to have similar ratios of thickness to amplitude and wavelength of corrugation (*h: a: λ*) as real blades from exposed sites. We combined measurements from Hurd and Pilditch (2011, shown in Table 1) and measurements from the *Macrocystis* blades shown in Fig. 1 ($h = 0.45$ mm, $a = 1.13$ mm, $\lambda = 5.0$ mm), which yielded $2.5 < a/h < 3$ and $6 < \lambda/h < 11$. The first corrugated model was designed with amplitude $a = 2.7h$ (2.0 ± 0.05 mm), which is in the middle of the range observed in the field. A second corrugated model was chosen with corrugation amplitude $a = 2h$ (1.5 ± 0.05 mm) to produce a dimensionless rigidity half way between the flat and fully corrugated models. The wavelength was set at $\lambda = 8h$ (= 6.0 ± 0.05 mm) for both corrugated blades, which is also in the middle of the observed range. The reported uncertainty corresponds to measurements of the final blade, which contributed to the uncertainty in η. For the flat blade, $\eta = 7.8 \pm 0.3 \times 10^{-6}$, calculated using Eqs. 1 and 2. For the corrugated blades, $\eta = 2.4 \pm 0.2 \times 10^{-4}$ and $\eta = 5.0 \pm 0.4 \times 10^{-4}$, for $a = 1.5$ mm and 2 mm, respectively, calculated from Eqs. 1 and 3.

The templates for laser cutting the blade molds were designed in Matlab. Each mold consisted of two acrylic plates out of which a sinusoidal topography was etched. Given the *x-y* resolution of the laser cutter (0.1 mm) and the wavelength $\lambda = 6.0$ mm, the corrugations for the models were created as discrete curves with 60 steps per wavelength. Visual inspection of the *Macrocystis* blade (Fig. 1) indicated that the blade thickness was uniform when measured perpendicular to the local blade surface (red line in Fig. 3), and this characteristic was preserved in the model blade. The surface arcs of the mold were constructed such that the perfect sinusoid was at the center of the blade (dashed black curve
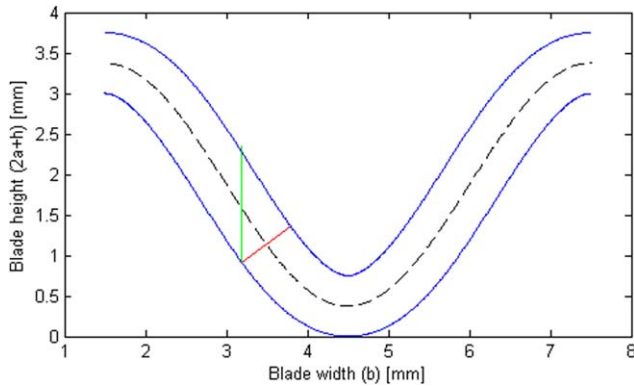
Fig. 3. Discrete curves representing one wavelength of the blade mold cross-section, which was $5\lambda = 3$ cm wide in total, for the model with corrugation amplitude $a = 1.5$ mm. A perfect sinusoid (dashed line) was aligned with the center of the blade. The top and bottom curves (blue lines) mark the templates for the acrylic molds. The red line shows the thickness of the blade measured perpendicular to the surfaces, while the green line shows the vertical displacement between the surfaces.

Fig. 4. (a) The grayscale templates created in Matlab with (b) the finished acrylic molds. The holes in the corners of the molds were drilled after laser cutting to help with alignment when filling the molds. The model blades were 3 cm wide (b) $\times$ 30 cm long (l), and each mold was 6 cm $\times$ 31.5 cm.

in Fig. 3). The upper and lower surfaces of the blade were one-half the thickness (h) above or below the sinusoidal curve, measured in the direction perpendicular to the center curve (e.g., red line in Fig. 3) at each discrete point.

The surface curves (blue lines in Fig. 3) were converted to values ranging from 0 to 255, and the discrete vectors were extended to create 2D matrices, which were finally converted to grayscale images. The grayscale images were used as templates for the laser cutter. The power and speed of the laser were set to etch a depth of twice the amplitude for black pixels. The laser then adjusted to a fraction of that power corresponding to the grayscale value (between 0 and 255) for non-black pixels. Examples of the template and acrylic plates are shown in Fig. 4.

The acrylic molds were cut leaving 1.5 cm of flat space along three sides of the blade area. This space was used to lay out metal spacers of the desired blade thickness ($h = 0.75$ mm). The bottom mold was filled with the VPS mixture (Fig. 5a), after which the top surface was screwed into place (Fig. 5b) and held down with weights while the polymer cured (20 min). Once cured, the top and bottom plates of the mold were unscrewed and carefully pried apart with a small flathead screwdriver. The polymer blade was peeled from the acrylic surface, and any excess polymer was cut away from the edges of the model blade. Separate acrylic molds were created and used for the two different corrugated models, and uncut plates of acrylic were used for the flat model. Figure 6 shows all of the completed blades.

Assessment

The three blades were tested in a water channel with a width of 38 cm and a water depth of 18 cm above a false bottom (Fig. 7). The blades were held in a horizontal posi-
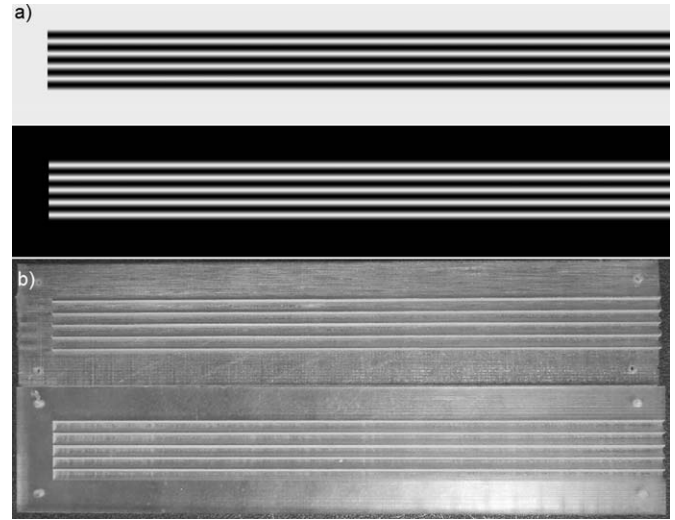
tion by a clamp at mid-depth. The current speed was 20 cm/s. Following Rominger and Nepf (2014), a vortex street was created by a 1-cm thick bar of height $D = 2.5$ cm that spanned the flume at mid-depth, which was aligned with the clamp and blade. While mimicking the interaction of the blades with individual turbulent eddies, the vortex street produced a single scale (bar height D) and frequency (1.2 Hz) that enabled simpler visualization and interpretation of the blade motion. The periodic eddies created by the bar had a wavelength of 4D. The upstream edge of the blade was placed 4D downstream from the bar.

Beneath the false bottom, the clamp was attached to a load cell (Futek LSB210) that measured the streamwise force on the clamp and blade. For each blade we reported the mean drag and the peak drag. Mean drag was calculated as an average over a 5 min long record collected at 2000 Hz, while peak drag was calculated as an average of the maximum drag measured in each vortex cycle. Additionally, we measured the force on the clamp without a blade and subtracted this value to isolate the force on the blade alone. The load cell was calibrated by measuring known weights incremented from 0 to 0.006 N, and the measurements were recorded using Labview software.

Videos were taken of each blade in the channel (using a Sony DFW-X710 camera). The videos were used to measure the average maximum vertical displacement of the blade tip per vortex cycle. The displacement measurements were calculated from 10 arbitrary one-cycle sequences for each blade. From each of 10 cycles, we recorded the maximum vertical displacement of the blade's tip (in either the upward or downward direction from the centerline) and then
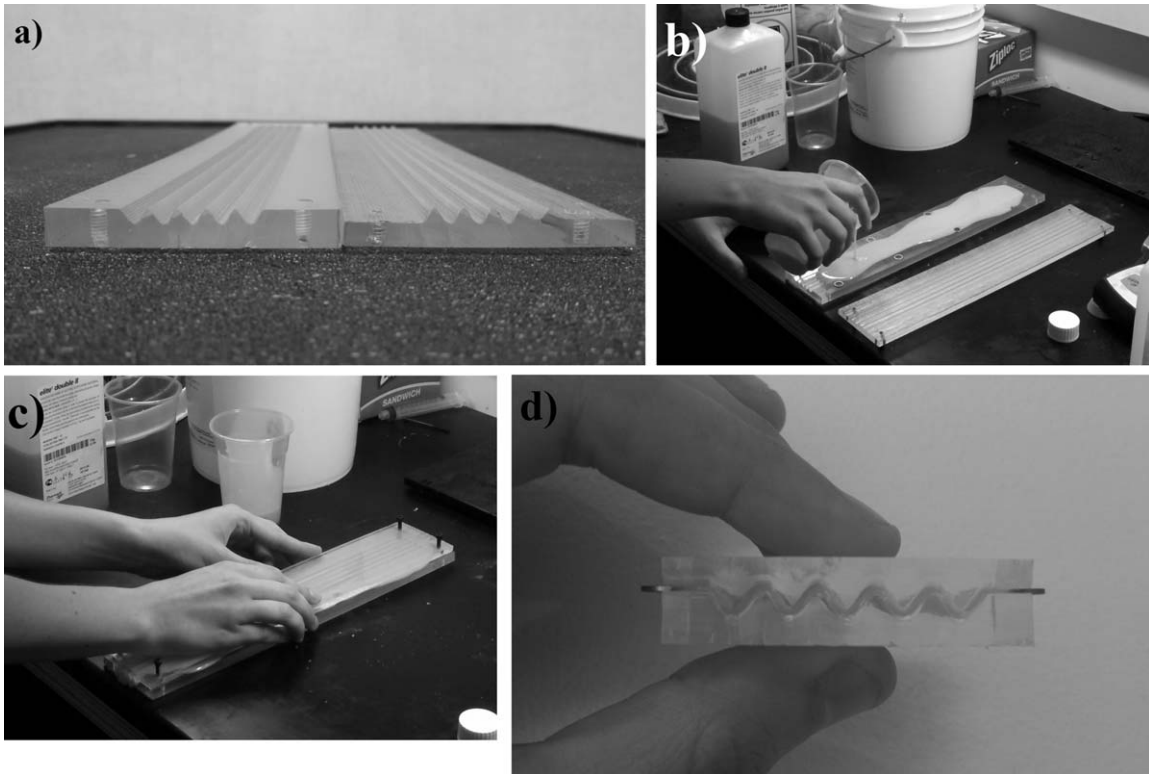
Fig. 5. Casting process using the laser-cut molds. (a) The acrylic molds were set on a table. Metal spacers were placed along the outer perimeter of the left mold to set the thickness, and (b) the prepared silicone mixture was poured onto the mold. (c) The mixture was covered with the right acrylic mold and held down with weights during curing (about 20 min). (d) A cross-sectional view of a 4 × 4 cm prototype mold filled with the VPS mixture.
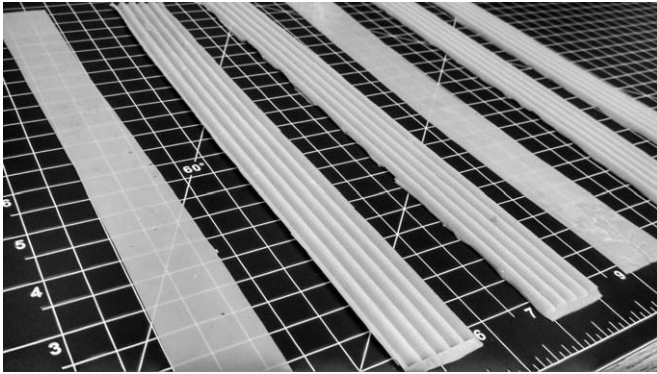

Fig. 6. Completed blades displayed here with duplicates (left to right: flat, $a = 1.5$ mm corrugated, $a = 2$ mm corrugated, flat, $a = 1.5$ mm corrugated, $a = 2$ mm corrugated). Each blade had an additional 1–2 mm of flat space at the end where the clamp attaches.

calculated the average over the 10 cycles. The vertical displacement was measured in Matlab by counting the number of pixels in the image between the centerline and the tip position and then converting to centimeters using the length of the clamp as calibration.

The measured drag force on the blades decreased significantly with the addition of corrugation (Fig. 8). Specifically, the mean drag on the corrugated blades was reduced relative to the flat blade by 12% and 35%, respectively for $a = 1.5$ mm and 2 mm (Fig. 8a). The maximum drag also decreased by similar percentages. Note that this drop in drag occurred despite an increase in surface area. The reduction in average drag per surface area relative to the flat blade was larger; 40% and 62%, respectively for $a = 1.5$ mm and 2 mm (Fig. 8b). The reduction in drag confirms that corrugations of the scale observed in the field can raise stiffness sufficiently to reduce by about 1/3 the total drag on individual blades.

The dependence of the blade motion on the level of corrugation was assessed qualitatively using video images. Figure 9 shows a video sequence for each of the three blades. The sequences are composed of five frames taken at intervals of 0.2 s, which represents approximately one cycle of vortex shedding. For a vortex shedding frequency of 1.2 Hz, one full period is ≈ 0.83 s. The flat blade (lowest η) experienced the greatest oscillation amplitude, or vertical displacement from the centerline. The downstream tip of the blade exhibited a maximum vertical displacement of 5.4 ± 0.3 cm from the neutral blade position, with the uncertainty representing the standard error measured over 10 sequences. The blade movement decreased with increasing corrugation amplitude. Specifically, the maximum tip excursion decreased to
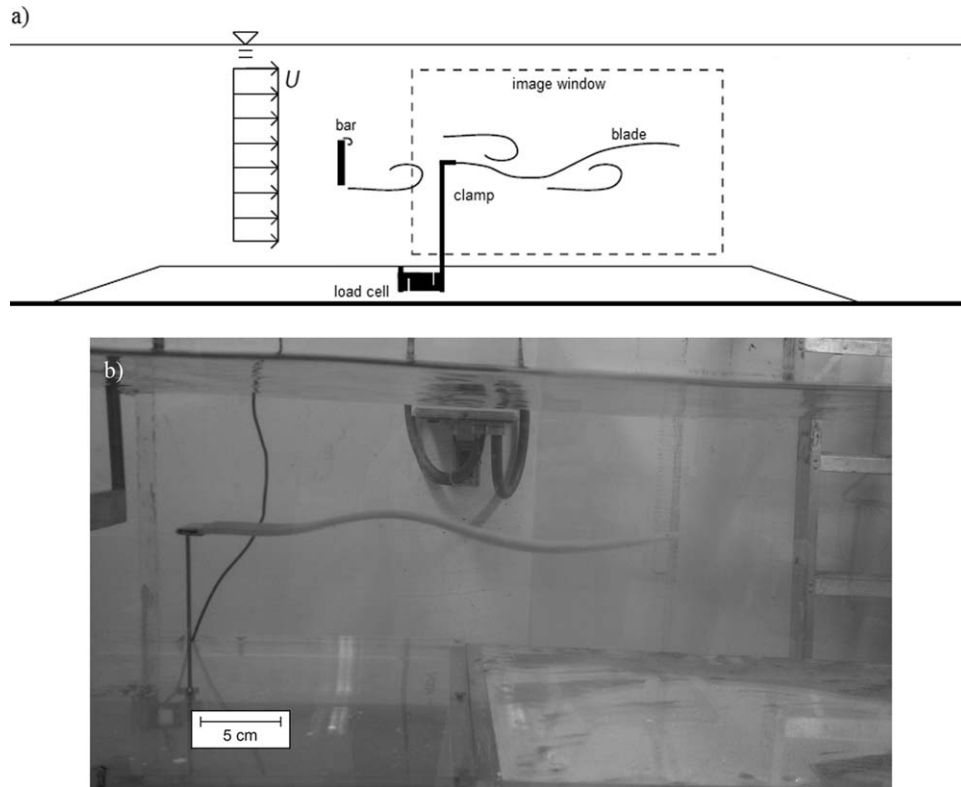
Fig. 7. (a) Schematic of experimental setup, which was the same as Rominger and Nepf (2014). (b) The $a = 1.5$ mm corrugated blade held horizontally in the channel by a narrow metal clamp, which was attached to the load cell beneath the false bottom.

3.0 ± 0.2 cm and 1.9 ± 0.2 cm for $a = 1.5$ mm ($\eta = 2.4 \times 10^{-4}$) and 2 mm ($\eta = 5.0 \times 10^{-4}$), respectively, representing a decrease of 44% and 65%, respectively, relative to the flat blade.

Our least rigid blade (flat blade, $\eta = 7.8 \times 10^{-6}$) exhibited the most asymmetric oscillations, meaning that the blade preferentially remained above or below the clamp centerline. For example, the sequence in Fig. 9a shows asymmetric oscillations favoring the downward direction. We quantified this asymmetry as the difference between the maximum upward and maximum downward displacement of the tip within each vortex period, normalized by the overall maximum displacement, and averaged this fraction over 10 cycles. An asymmetry of zero indicates equal displacement up and down (perfect symmetry) while 1 is the maximum asymmetry. The asymmetry of the flat blade and the 1.5 mm and 2 mm corrugated blades was 0.67 ± 0.06, 0.56 ± 0.07, and 0.42 ± 0.08, respectively, indicating that asymmetry decreased with increasing blade rigidity.

Discussion

The addition of 2 mm corrugation reduced the drag per surface area by 62% (Fig. 8b). This is a much larger reduction in drag than can be attributed to the impact of corrugation on skin friction (8%, Djenidi et al. 1994). This suggests that the reduction in blade motion and associated reduction in tensile forces make a greater contribution to overall drag reduction than the reduction in skin friction. Over a similar change in dimensionless blade rigidity ($\eta = 5 \times 10^{-6}$ to $\eta = 5 \times 10^{-4}$, between the flat and 2 mm corrugated blade), Rominger and Nepf observed a 45% reduction in drag (2014). Because surface area was constant in their experiments, the reduction in drag per surface area was the same (45%). This falls between our observed reduction in drag (35%) and drag per surface area (62%). Further, Rominger and Nepf (2014) observed a similar reduction in vertical displacement for blades with increasing blade rigidity. Specifically, they observed a change in rms-vertical displacement from 2.5 cm ($\eta \approx 10^{-6}$) to 0.5 cm ($\eta \approx 4 \times 10^{-4}$), representing a decrease of 80%, comparable to the 65% decrease observed in this study. The general agreement in the magnitude of drag and blade motion reduction over a similar increase in dimensionless rigidity (η) suggests that this parameter (η) works universally for rigidity associated with blade thickness or with blade morphology (here, corrugations). Finally, in this study the least rigid blade (flat blade, $\eta = 7.8 \times 10^{-6}$) exhibited the greatest asymmetry in motion. Rominger and Nepf (2014) also noted asymmetric blade motion for $\eta < 1 \times 10^{-4}$, with asymmetry increasing with decreasing rigidity. They showed that the asymmetric
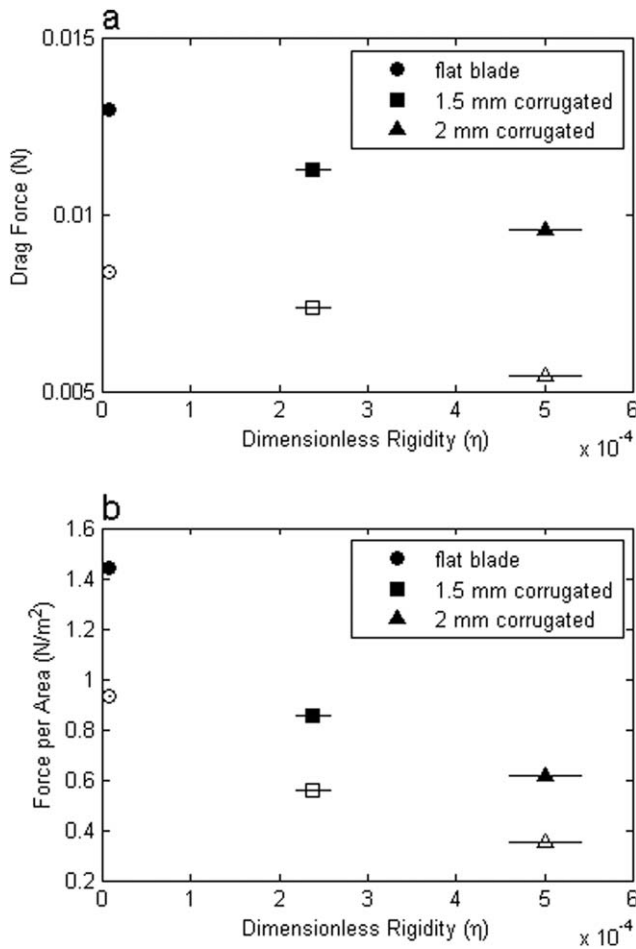
Fig. 8. (a) The measured drag force and (b) the drag force per surface area as a function of dimensionless blade rigidity. For each blade, the solid markers represent the maximum drag force while the open markers represent the average drag force. The standard error in the time-averaged drag measurements is within the size of the symbols shown. The uncertainty in the η measurements is represented by the black horizontal lines. The uncertainty in the flat blade's rigidity is within the size of the symbol.

motions were associated with enhanced acceleration at the tip and an elevation in peak drag force.

The drag measurements made in this study demonstrate that corrugations of the scale observed in the field can raise stiffness sufficiently to reduce by one-third the drag on individual blades. Decreasing drag protects the plant from being dislodged or torn. To extrapolate to field conditions, the measured forces (F) were converted to a drag coefficient, $C_D = F/(\rho_f b l U^2)$. For the flat blade and 2 mm corrugated blade, $C_D = 0.035$ and 0.025, respectively. Because the models were geometrically and dynamically scaled to real blades, the drag coefficients can be used to estimate forces in the field. Using the average dimensions reported by Hurd and Pilditch (2011) for *Macrocystis* blades in an exposed region ($L = 0.62$ m, $b = 0.056$ m, $h = 5 \times 10^{-4}$ m) and a representative current speed of 1 m/s, the maximum force on the flat and corrugated

blade would be 1.2 N and 0.86 N, respectively. These correspond to a peak stress of 0.43×10^5 Nm^{-2} and 0.31×10^5 Nm^{-2}. While the peak stress is reduced for the corrugated blade, both values fall below the observed breaking stress reported for *Macrocystis* blades (Table 2.2 of Hale 2001, $\sigma_{\text{br}} = 7.8 \pm 1.3 \times 10^5$ Nm^{-2}). The advantage provided by corrugations would become significant relative to breakage near 4 ms^{-1}, which would likely be associated with a combination of waves and current, for which the flat blade stress would reach the breaking limit (6.9×10^5 Nm^{-2}), but the corrugated blade would remain safely below it (4.9×10^5 Nm^{-2}).

Rominger and Nepf (2014) identified the following trade-off with blade stiffness: stiffer blades have the positive influence of decreasing drag, but the negative influence of decreasing flux to the blade surface, because stiffer blades experience less relative motion between the water and blade surface. This trade off points to a possible benefit of corrugation over increased blade thickness as a mechanism for providing enhanced rigidity. Nutrient uptake is a function of the surface area of the blade. Developing corrugations maintains a constant surface area to volume ratio, whereas increasing thickness decreases this ratio, which can diminish nutrient flux per blade volume.

Longitudinal corrugations are often associated with exposed sites, where water motion associated with waves and currents reduces the thickness of the diffusive boundary layer, facilitating flux to the blade (e.g., Hurd et al. 1996; Hurd 2000; Hurd and Pilditch 2011). Consistent with this, Hepburn et al. (2007) observed a correlation between *Macrocystis* blade growth and current/wave exposure during seasons when tissue nitrogen levels were low. Specifically, higher growth rates were observed at exposed sites, compared to sheltered sites, consistent with a higher nutrient flux. Similarly, Stewart et al. (2009) observed higher growth rates at the edge of a dense kelp bed, where the current exposure was higher, than in the middle, where the current was reduced to 25% of the edge current. Stephens and Hepburn (2014) also attribute observed spatial variation in uptake and growth rates across a kelp bed to variation in current and wave exposure between the edge and interior of the bed. In addition, under some high-flow conditions the rate at which nutrients are delivered to the blade surface may be so rapid as to no longer be limiting, and the nutrient uptake by kelp will instead be limited by physiological controls—how fast the kelp can store or use nutrients (Gerard 1982a,b). These scenarios all suggest that in high flow environments the possible decrease in the nutrient delivery caused by increased stiffness (corrugations) may not be detrimental to blade survival, because the flux is already high or not limiting. At the same time, the decrease in drag (drag coefficient) associated with increased stiffness (corrugations) would be a greater benefit in high-flow environments, because drag increases with current speed squared. This may explain why corrugations are observed at exposed sites. In contrast, other species of kelp exhibit a different morphological shift in
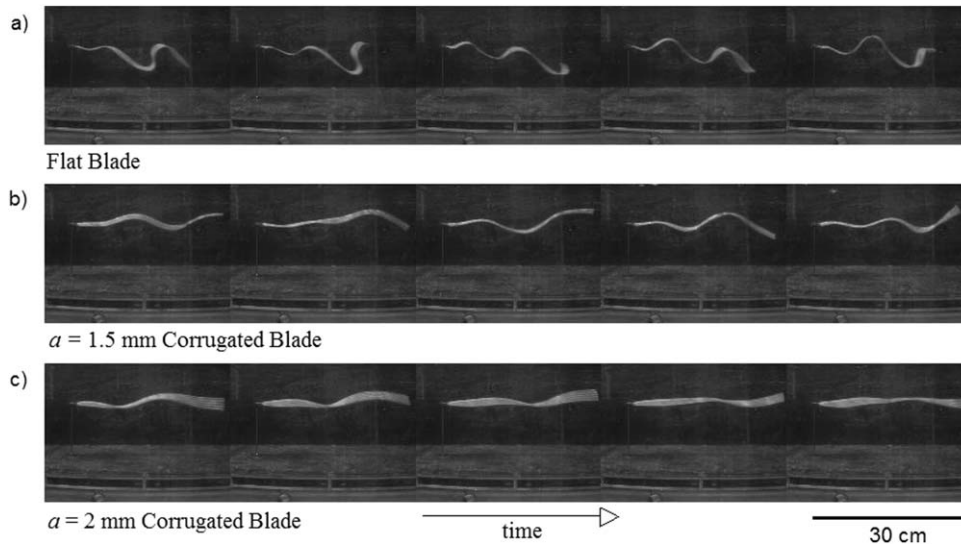
Fig. 9. (a) Flat blade, (b) 1.5 mm amplitude corrugation, (c) 2 mm amplitude corrugation. Each sequence represents one cycle of vortex shedding. The frequency of vortex shedding from the $D = 2.5$ cm bar was 1.2 Hz, which yielded a period of 0.83 s. The five frames in each of the above sequences are spaced 0.2 s apart ($^1/_4$ the period).

Fig. 10. The image on the left shows one example of random corrugation peaks, and the image on the right is the resulting grayscale template.

response to the trade-off between drag and nutrient flux. For example, *Laminaria saccharina* and *Nereocystis luetkeana* blades have ruffles along their edges in sheltered regions but are flat in exposed regions. The ruffles increase blade movement, which is a benefit in low flow environments, because at currents speeds experienced at sheltered sites the blade motion enhances nutrient flux (Koehl and Alberte 1988; Huang et al. 2011). However, for a given current speed, the ruffled blade experiences a higher drag than the flat morphology, so that the flat blade provides a drag benefit in high current environments (Koehl and Alberte 1988).

More complex morphologies can also be created with the fabrication method described here. For example, the actual corrugations in nature are not perfect sinusoids, as we modeled them here (Fig. 4), but have curved peaks and valleys and begin and end at random locations along the length of the blade (Fig. 1). To create templates for more realistic corrugations, we began with a distribution of peak lines based on tracings of real blades (Fig. 10a). A Matlab code filled in a linear vertical gradient where each peak line ended and a horizontal sinusoidal gradient between adjacent peaks. An example of peak lines converted to a grayscale template is given in Fig. 10b. Finally, our blade fabrication method can be used to build a canopy of kelp blades to consider how blade stiffness (gained either through blade thickness or corrugation) influences the interactions between multiple blades. Kelp blades do not exist in isolation in nature, and when the blades become

entangled, they are at higher risk of breakage. The new models could be used to explore whether increased rigidity reduces entanglement between blades. Changes in blade rigidity may also impact light availability, and thus photosynthesis within a canopy. For example, within a *Macrocystis* bed, light penetration to the understory can be limited by interception in the upper canopy (Reed and Foster 1984; Watanabe et al. 1992). Less rigid blades, which move more freely, might produce more even light conditions within and below the canopy, because the movement of blades keeps any individual blade from being shaded for an extended period of time, e.g., as shown for wave-induced motion of kelp blades (Wing et al. 1993). Alternatively, the light absorption of an individual blade is related to its projected horizontal area. More rigid blades maintain a more horizontal position in flow (Fig. 9), which may provide an advantage in light capture and photosynthesis.

References

Briassoulis, D. 1986. Equivalent orthotropic properties of corrugated sheets. Comput. Struct. **23**: 129–138. doi:10.1016/0045-7949(86)90207-5

Denny, M., B. Gaylord, B. Helmuth, and T. Daniel. 1998. The menace of momentum: Dynamic forces on flexible organisms. Limnol. Oceanogr. **43**: 955–968. doi:10.4319/lo.1998.43.5.0955

Denny, M., and L. Roberson. 2002. Blade motion and nutrient flux to the kelp *Eisenia arborea*. Biol. Bull. **203**: 1–13. doi:10.2307/1543453

Djenidi, L., E. Anselmet, J. Liandrat, and L. Fulachier. 1994. Laminar boundary layer over riblets. Phys. Fluids **6**: 2993–2999. doi:10.1063/1.868429

Druehl, L., and L. Kemp. 1982. Morphological and growth responses of geographically isolated *Macrocystis integrifolia* populations when grown in a common environment. Can. J. Bot. **80**: 1409–1413. doi:10.1139/b82-179

Gerard, V. 1982a. In situ rates of nitrate uptake by giant kelp, *Macrocystis pyrifera* (l.) c. agardh: Tissue differences, environmental effects, and predictions of nitrogen-limited growth. J. Exp. Mar. Biol. Ecol. **62**: 211–224. doi:10.1016/0022-0981(82)90202-7

Gerard, V. 1982b. In situ water motion and nutrient uptake by the giant kelp *Macrocystis pyrifera*. Mar. Biol. **69**: 51–54. doi:10.1007/BF00396960

Hale, B. 2001. Macroalgal materials: Foiling fracture and fatigue from fluid forces. Ph.D. thesis. Stanford University.

Hepburn, C., J. Holborow, S. Wing, R. Frew, and C. Hurd. 2007. Exposure to waves enhances the growth rate and nitrogen status of the giant kelp *Macrocystis pyrifera*. Mar. Ecol. Prog. Ser. **339**: 99–108. doi:10.3354/meps339099

Huang, I., J. Rominger, and H. Nepf. 2011. The motion of kelp blades and the surface renewal model. Limnol. Oceanogr. **56**: 1453–1462. doi:10.4319/lo.2011.56.4.1453

Hurd, C. 2000. Water motion, marine macroalgal physiology, and production. J. Phycol. **36**: 453–472. doi:10.1046/j.1529-8817.2000.99139.x

Hurd, C., P. Harrison, and L. Druehl. 1996. Effect of seawater velocity on inorganic nitrogen uptake by morphologically distinct forms of *Macrocystis integrifolia* from wave-sheltered and exposed sites. Mar. Biol. **126**: 205–214. doi:10.1007/BF00347445

Hurd, C., and C. Pilditch. 2011. Flow-induced morphological variations affect diffusion boundary-layer thickness of *Macrocystis pyrifera* (heterokontophyta, laminariales). J. Phycol. **47**: 341–351. doi:10.1111/j.1529-8817.2011.00958.x

Hurd, C., C. Stevens, B. Laval, G. Lawrence, and P. Harrison. 1997. Visualization of seawater flow around morphologically distinct forms of the giant kelp *Macrocystis integrifolia* from wave-sheltered and exposed sites. Limnol. Oceanogr. **42**: 156–163. doi:10.4319/lo.1997.42.1.0156

Koehl, M., and R. Alberte. 1988. Flow, flapping, and photosynthesis of *Nereocysis luetkeana*: A functional comparison of undulate and flat blade morphologies. Mar. Biol. **99**: 435–444. doi:10.1007/BF02112137

Koehl, M., W. Silk, H. Liang, and L. Mahadevan. 2008. How kelp produce blade shapes suited to different flow regimes: A new wrinkle. Integr. Comp. Biol. **48**: 834–851. doi:10.1093/icb/icn069

Lau, J. 1981. Stiffness of corrugated plate. J. Eng. Mech. Div. **107**: 271–275.

Michelin, S., S. L. Smith, and B. Glover. 2008. Vortex shedding model of a flapping flag. J. Fluid Mech. **617**: 1–10. doi:10.1017/S0022112008004321

Norton, T. A. 1969. Growth form and environment in *Saccorhiza polyschides*. J. Mar. Biol. Assoc. UK **49**: 1025–1045. doi:10.1017/S0025315400038078

Reed, D., and M. Foster. 1984. The effect of canopy shading on algal recruitment and growth in a kelp forest. Ecology **65**: 937–948. doi:10.2307/1938066

Rominger, J., and H. Nepf. 2014. Effects of blade flexural rigidity on drag force and mass transfer rates in model blades. Limnol. Oceanogr. **59**: 2028–2041. doi:10.4319/lo.2014.59.6.2028

Rosman, J., M. Denny, R. Zeller, S. Monismith, and J. Koseff. 2013. Interaction of waves and currents with kelp forests (*Macrocystis pyrifera*): Insights from a dynamically scaled laboratory model. Limnol. Oceanogr. **58**: 790–802. doi:10.4319/lo.2013.58.3.0790

Stephens, T., and C. Hepburn. 2014. Mass-transfer gradients across kelp beds influence *Macrocystis pyrifera* growth over small spatial scales. Mar. Ecol. Prog. Ser. **515**: 97–109. doi:10.3354/meps10974

Stewart, H., J. Fram, D. Reed, S. Williams, M. Brzezinski, S. MacIntyre, and B. Gaylord. 2009. Differences in growth, morphology and tissue carbon and nitrogen of *Macrocystis pyrifera* within and at the outer edge of a giant kelp forest

in California, USA. Mar. Ecol. Prog. Ser. **375**: 101–112. doi:10.3354/meps07752

Watanabe, J., R. Phillips, N. Allen, and W. Anderson. 1992. Physiological response of the stipitate understory kelp *Pterygophora californica* Ruprecht, to shading by the giant kelp, *Macrocystis pyrifera* C. Agardh. J. Exp. Mar. Biol. Ecol. **159**: 237–252. doi:10.1016/0022-0981(92)90039-D

Wing, S., J. Leichter, and M. Denny. 1993. A dynamic model for wave-induced light fluctuations in a kelp forest. Limnol. Oceanogr. **38**: 396–407. doi:10.4319/lo.1993.38.2.0396